Numerical relativity simulations of prompt collapse mergers: Threshold mass and phenomenological constraints on neutron star properties after GW170817

Rahul Kashyap,[1,2,*] Abhishek Das,[1,2] David Radice,[1,2,3] Surendra Padamata,[1,2] Aviral Prakash,[1,2] Domenico Logoteta,[4,5] Albino Perego,[6,7] Daniel A. Godzieba,[2] Sebastiano Bernuzzi,[8] Ignazio Bombaci,[4,5] Farrukh J. Fattoyev,[9] Brendan T. Reed,[10] and André da Silva Schneider[11]

[1]*Institute for Gravitation and the Cosmos, The Pennsylvania State University, University Park, Pennsylvania 16802, USA*
[2]*Department of Physics, The Pennsylvania State University, University Park, Pennsylvania 16802, USA*
[3]*Department of Astronomy and Astrophysics, The Pennsyvlania State University, University Park, Pennsylvania 16802, USA*
[4]*Dipartimento di Fisica, Università di Pisa, Largo B. Pontecorvo, 3 I-56127 Pisa, Italy*
[5]*INFN, Sezione di Pisa, Largo B. Pontecorvo, 3 I-56127 Pisa, Italy*
[6]*Dipartimento di Fisica, Università di Trento, Via Sommarive 14, 38123 Trento, Italy*
[7]*INFN-TIFPA, Trento Institute for Fundamental Physics and Applications, ViaSommarive 14, I-38123 Trento, Italy*
[8]*Theoretisch-Physikalisches Institut, Friedrich-Schiller Universität Jena, 07743 Jena, Germany*
[9]*Department of Physics, Manhattan College, Riverdale, New York 10471, USA*
[10]*Department of Astronomy, Indiana University, Bloomington, Indiana 47405, USA*
[11]*The Oskar Klein Centre, Department of Astronomy, Stockholm University, AlbaNova, SE-106 91 Stockholm, Sweden*

(Received 12 November 2021; accepted 30 March 2022; published 20 May 2022)

We determine the threshold mass for prompt (no bounce) black hole formation in equal-mass neutron star (NS) mergers using a new set of 227 numerical relativity simulations. We consider 23 phenomenological and microphysical finite-temperature equations of state (EOS), including models with hyperons and first-order phase transitions to deconfined quarks. We confirm the existence of EOS-insensitive relations between the threshold mass, binary tidal parameter at the threshold ($\Lambda_{\rm th}$), maximum mass of nonrotating NSs, and radii of reference mass NSs. We combine the EOS-insensitive relations, phenomenological constraints on NS properties, and observational data from GW170817 to derive an improved lower limit on radii of maximum mass and a 1.6 $M_\odot$ NS of 9.81 and 10.90 km, respectively. We also constrain the radius and quadrupolar tidal deformability (Λ) of a 1.4 $M_\odot$ NS to be larger than 10.74 km and 172, respectively. We consider uncertainties in all independent parameters—fitting coefficients as well as GW170817 masses while reporting the range of radii constraints. We discuss an approach to constrain the upper as well as lower limit of NS maximum mass using future binary NS detections and their identification as prompt or delayed collapse. With future observations, it will be possible to derive even tighter constraints on the properties of matter at and above nuclear density using the method proposed in this work.

DOI: 10.1103/PhysRevD.105.103022

I. INTRODUCTION

Binary neutron star (BNS) mergers are one of the most important events in gravitational wave astronomy. At least two such events have been detected by LIGO and Virgo thus far (namely, GW170817 [1] and GW190425 [2]). Apart from gravitational waves, BNS mergers may produce electromagnetic (EM) counterparts across the entire EM spectrum, which can be detected by various space- and ground-based observatories. These events result in one of the following two outcomes. The merger remnant may be a massive, differentially rotating neutron star secured by centrifugal and thermal effects that possibly collapses to a black hole on a dynamical or secular timescale. Material that becomes gravitationally unbound during the coalescence undergoes rapid neutron-capture nucleosynthesis and contribute to the galactic enrichment by heavy elements. The energy released by the radioactive decay of the nucleosynthesis products power electromagnetic counterparts, called kilonova [3–9]. Alternatively, the remnant may form a black hole immediately upon merger, the so-called prompt collapse. In this case, if the stars have comparable

*rkk5314@psu.edu

 © 2022 American Physical Society

masses, most of the matter falls immediately into the black hole, resulting in an EM-quiet merger, so the occurrence of prompt collapse can be determined with multimessenger observations [10–16]. Bright electromagnetic counterparts might still be expected for high mass-ratio prompt collapse binaries [17]. This study is concerned with the binary threshold mass M_{th} that separates these two outcomes for equal-mass binaries.

The phenomenon of prompt collapse has been investigated by several groups [10,11,18–22]. It is widely accepted that the threshold mass for prompt collapse should be strongly correlated with other physical properties of the equation of state (EOS). This can be used to place constraints on the EOS using information from future possible observations of prompt and/or delayed collapse. Shibata *et al.* [10] first proposed that the minimum total mass of binary undergoing prompt collapse is directly proportional to the maximum mass M_{max} of cold nonrotating neutron stars (NSs). This was later corroborated with an extensive study spanning multiple EOS by Hotokezaka *et al.* [11]. Bauswein *et al.* [18] extended the theoretical correlation study by proposing a further linear relationship between the compactness of the maximum mass neutron star ($C_{max} = GM_{max}/R_{max}c^2$, where G is Newton's gravitational constant, c is the speed of light, M_{max} and R_{max} are the mass and radius of the maximum mass NS) and the proportionality constant ($k_{th} = M_{th}/M_{max}$) between the threshold mass (M_{th}) and maximum mass (M_{max}). They also found new EOS-insensitive relations between k_{th} and other quantities depending on the EOS, such as with the modified compactness $C^*_{1.6}(= GM_{max}/c^2R_{1.6}$, where $R_{1.6}$ is the radius of a 1.6 $M_\odot$ NS) [18], radii, and quadrupolar tidal polarizability parameter [23] (hereafter, shortly, tidal deformability) (Λ) at few particular values of masses [22]. Since GW170817 had a bright EM counterpart [24], it is widely believed not to have been a prompt collapse event, e.g., [25]. Using this information and the proposed correlations between k_{th} and $C^*_{1.6}$, Bauswein *et al.* [26] have derived a lower limit for $R_{1.6}$, the radius of a cold 1.6 $M_\odot$ NS. Köppel *et al.* [20] have used a nonlinear fit between M_{max} and M_{th} motivated by the condition that $k_{th} \to 0$ as compactness reaches that of black hole (BH). They derive a lower limit of radii as a function of NS masses later extended by [27] to asymmetric binaries. Agathos *et al.* [28] presented a Bayesian framework based on these correlations to calculate the probability of prompt collapse for a given merger from the inspiral gravitational wave (GW) signal. More recently, Bauswein *et al.* [21,22] have considered the effect of mass-ratio and phase transitions. They claimed that the combined measurement of M_{th} and the binary tidal parameter of the corresponding binary $\tilde{\Lambda}_{th}$ could reveal the presence of QCD phase transitions in cold, dense matter. In particular, they identified a region in the $M_{th} - \tilde{\Lambda}_{th}$ plane that was only populated by EOS models with strong first-order phase transitions. They argued that, should the observationally determined M_{th} and $\tilde{\Lambda}_{th}$ lay in this region, this would be smoking gun evidence for a phase transition.

Recently, several studies have investigated the impact of mass ratio on the M_{th} [22,27,29,30]. Bauswein *et al.* [22] have found that the M_{th} may decrease or increase for asymmetric systems depending upon the stiffness of EOS. In Bauswein *et al.* [22], a fitting formula of the difference is provided with respect to the nonrotating NS properties along with an explanation of this difference using the angular momentum of binaries. Using the fitting procedure of Köppel *et al.* [20], Tootle *et al.* [27] have extended their earlier studies by looking at the impacts of mass ratio and spin. Perego *et al.* [29] have looked at the effect of mass ratio and provided an explanation from the fundamental perspective of nuclear physics and angular momentum of binaries. They provide a broken linear fit of M_{th} with respect to mass ratio in two regimes (lower and higher than $q = 0.725$) and incompressibility at the maximum NS density (K_{max}), fundamental to the behavior of EOS. They further provide a method to constrain the K_{max} by observing the difference of M_{th} between symmetric and nonsymmetric BNS systems. Kölsch *et al.* [30] discusses the impact of asymmetry by introducing an extended version of the fitting formula from Bauswein *et al.* [22] to account for the different behaviors in two regimes of mass ratio and for different EOS. There is an agreement among these studies that, while spin can increase the threshold mass by 5%–10%, the effect of large asymmetry is to decrease the threshold mass by up to 8% for most of the EOS. However, there are few EOS for which M_{th} increases for intermediate mass ratios [29].

In this work, we revisit the issue of the prompt BH formation in binary NS mergers. On one hand, we confirm the existence of EOS-insensitive relations between k_{th} and other parameters that depend on the EOS. On the other hand, we find small, but statistically significant, systematic deviations between our results, obtained with full general relativity simulations, and those of Bauswein *et al.* [18] that used approximate general relativity simulations. However, we find our linear fit to be in closer agreement with Bauswein *et al.* [22] with differences for data points at higher values of C_{max}. Our results are consistent with those obtained by other groups also performing general relativity simulations. We extend the methods of Bauswein *et al.* [26] to combine observational data and simulation results and derive updated constraints on the radius of 1.4 $M_\odot$ and 1.6 $M_\odot$ NSs, as well as on the radius of the maximum mass NS. We also reexamine the claim of Bauswein *et al.* [21,22] that a particular combination of values of M_{th} and Λ_{th} would imply the presence of a first-order phase transition in the core of NSs. We find consistency with their claim for most of the EOS, however, the error bars on Λ_{th} (the tidal deformability of a NS with mass equal to half of M_{th}) of few nucleonic EOS shows large uncertainties

requiring future high resolution studies to confirm or refute their hypothesis.

In the next section, we describe the EOS models used in our simulation classified into different categories. We describe the details of numerical simulations and the method to identify prompt collapse in Sec. III. Further, we describe three main classes of outcomes from BNS mergers using the midplane rest mass density slices and time series of key physical quantities in Sec. IV. In the same section, we describe the correlation between M_{th} and M_{max}, the phenomenological constraints on NS properties, and derive constraints on M_{max}, radii, and M_{th} using the correlations. Finally, we provide a brief conclusion of our results in Sec. V.

II. EQUATION OF STATE

In the present work, we consider a set of 23 EOS models. This set includes (a) 21 composition-dependent EOS derived using different frameworks to describe the many-body dynamics of the stellar constituents and (b) two entirely phenomenological zero-temperature piecewise polytropic EOS from [31].

Fifteen EOS of the subset (a) are nucleonic models, i.e., they include only neutrons and protons as hadronic components of dense matter. More specifically, the nucleonic EOS we consider are BLh [32,33], HS(DD2) [34,35], LS220 [36], SFHo [37], SRO(SLy) [38,39], nine variants of the SRO EOS with different values of the empirical nuclear parameters [39,40], and the big apple EOS (BA from now on) [41]. With the exception of the BA EOS, all these models are finite-temperature EOS, i.e., thermal effects are consistently calculated within the adopted many-body framework. Three EOS models include hyperons in addition to nucleons: HS (BHB$\Lambda\phi$, just BHB elsewhere in this paper) [42], H3, and H4 [43–45]. The latter two are zero-temperature models. Finally, we consider three EOS models that include a transition to a phase with deconfined quark: the finite-temperature BLQ [46] and DD2qG (Logoteta *et al.* [47]) EOS and the zero-temperature ALF2 [48] EOS. In the BLQ EOS the nucleonic phase is described by the BLh model [32,33], while the quark phase is described by an extended version of the phenomenological bag model EOS, which includes the effects of gluon mediated QCD interactions between quarks up to the second order in the QCD coupling α_s [49–51]. The nucleonic and the quark phase are then joint assuming a first-order phase transition according to the so-called Gibbs construction [52]. The possibility of a quark deconfinement phase transition is again considered in the DD2qG and ALF2 EOS models and the Gibbs construction is still adopted in both cases to join the hadronic and the quark phases. For the latter phase, in the case of the DD2qG, the same quark model used for the BLQ EOS is employed, while in ALF2 the quark model was extended to include the effect of color superconducting assuming a color-flavor-locked quark phase [48].

Finally, we include thermal effects in the zero-temperature EOS models (BA, H3, H4, ALF2, and piecewise polytropic EOS from subset (b), GRW1 and GRW2) by adding a thermal contribution with adiabatic index $\Gamma_{th} = 1.7$ following, e.g., Refs. [10,53–55], see [56,57] for an alternative approach.

The mass radius curves for nonrotating neutron stars obtained for all the considered EOS models are shown in Fig. 1.

III. NUMERICAL SIMULATIONS

We construct irrotational quasicircular binary initial data with the pseudospectral code LORENE [58]. The initial separation between the centers of the two stars is typically taken to be 40 km, the exception being the BLh initial data, used for both the BLh and BLQ binaries, for which the initial separation is 45 km [46]. Evolutions are carried out with the WhiskyTHC code [15,59–64], which is built on top of the EINSTEIN TOOLKIT [65]. Our simulations make use of the CARPET adaptive mesh refinement framework [66,67], which implements the Berger-Oliger scheme with refluxing [68,69]. We use seven levels of mesh refinement, with the finest grid covering the NSs and the merger remnant entirely. Our fiducial simulations, referred to as the standard resolution (SR), have a resolution of $0.125\ GM_\odot/c^2 \simeq 185$ m. Additional simulations are performed at the lower resolution (LR) of $0.167\ GM_\odot/c^2 \simeq 246$ m for all the binaries near the threshold mass. The grid setup is discussed in detail in Ref. [15]. Simulations performed with microphysical EOS also account for neutrino emission using the leakage scheme discussed in [63,70].

We define a binary to have undergone prompt collapse if the remnant does not bounce back after merger and instead a BH is immediately formed. We remark that this definition has been used in most previous studies, e.g., [11,16,18], with the notable exceptions of Köppel *et al.* [20] and Tootle *et al.* [27], which instead use a condition based on the time for the formation of a BH after merger. As in most previous studies, but again differently from Köppel *et al.* [20], the BH formation threshold is obtained using a bracketing procedure. Köppel *et al.* [20] used an extrapolation method to identify M_{th}. For most EOS, we are able to determine M_{th} to within $0.05\ M_\odot$. For those EOS for which we find discrepancies between standard and low resolution simulations (BA, DD2, SRO5, and SFHo), we have reported the threshold masses corresponding to both resolutions in Table I. In our analysis, we have used SR results, but we have extended the error bars to account for this discrepancy. Additionally, we have checked that our results are robust, to within the estimated errors, with respect to changes in the gauge conditions for the BLQ equation of state, where the difference between Gamma and integrated Gamma driver (GD and IGD, respectively) gauge conditions [71,72] is equal to the error bar in M_{th} and is nonexistent for BLh.

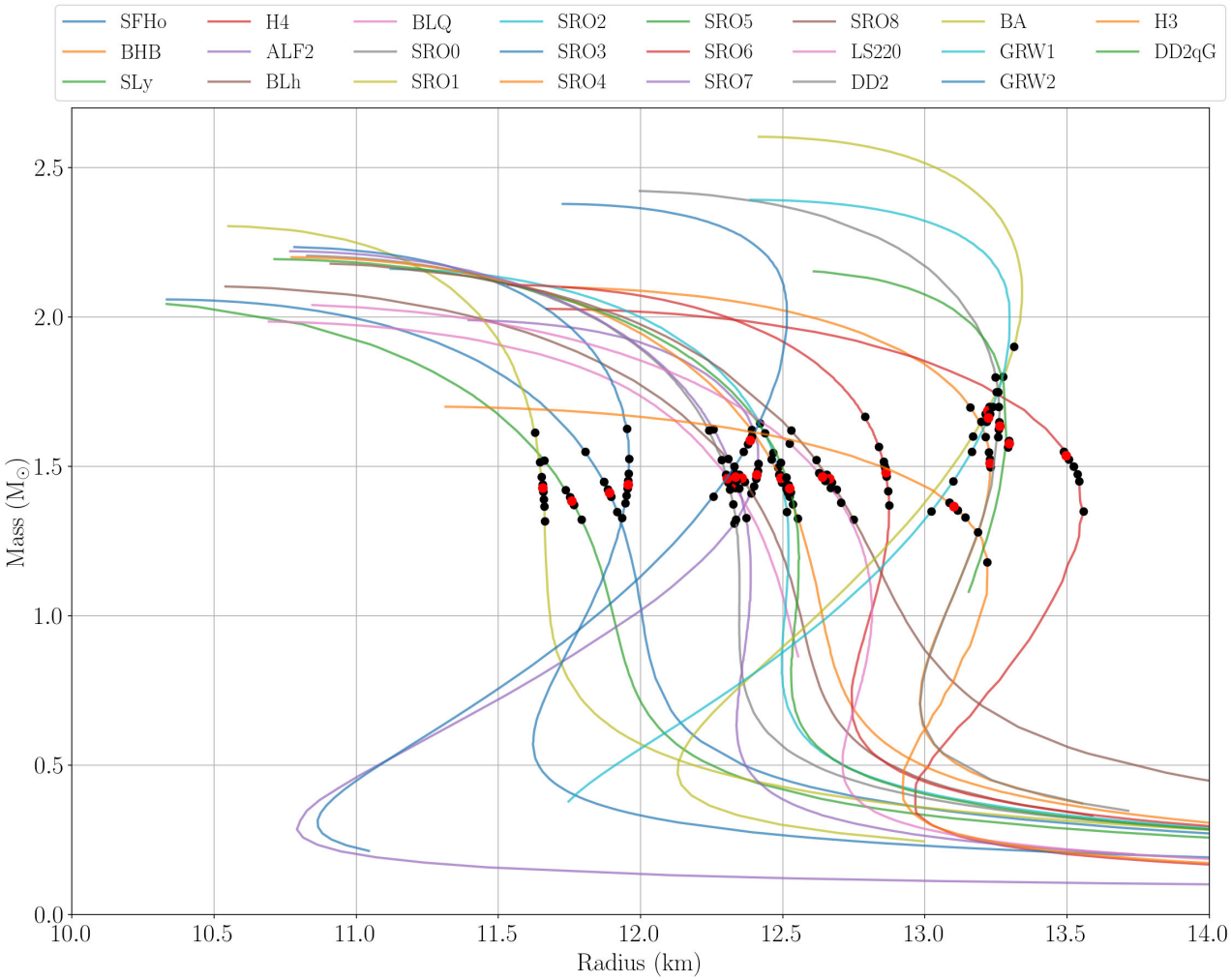

FIG. 1. Mass-radius curves for the equations of state used in our simulations. The dots indicate component masses and radii for binaries that we simulated, the red ones denote the minimum mass binaries that underwent prompt collapse.

Overall, we have performed 227 numerical relativity simulations for this study.

IV. RESULTS

In Fig. 2, we show slices of the rest mass density on the orbital plane from three different binaries representative of typical outcomes. We chose EOS SRO2 for this demonstration. Moreover, in slices where the value of the lapse function drops below 0.2, we have included a contour indicating the spatial location where it happens. This is a rough estimate of the apparent horizon and the appearance of this contour indicates that the merger remnant has collapsed and formed a black hole [17].

The first row of Fig. 2, involving stars of gravitational mass 1.35 $M_\odot$ each, presents a merger resulting in a long-lived merger remnant (or a massive NS). The left panel shows the moment just after the merger as the two NSs make contact. The second panel demonstrates a merger remnant with a double core structure surrounded by a common envelope. The third and final panel shows a single rotating neutron star with an oscillating core, losing energy and angular momentum through the emission of gravitational waves to achieve greater stability more than 10 ms after the merger. For the minimum lapse, maximum of the rest mass density, and gravitational wave strain as a function of time, see the first column of Fig. 3.

The second row of Fig. 2 shows a binary of component mass 1.45 $M_\odot$, which undergoes delayed collapse. Like in the previous case, the left panel represents the remnant just after merger. Plumes of ejecta can be seen emerging as the remnant spins with the residual angular momentum of the merged binary. In the middle panel, the core of the remnant has already collapsed as indicated by the lapse decreasing below 0.2 and ejection of the outer layers of matter continues to take place. The right panel shows the remnant after most of the matter has either been ejected or accreted onto the black hole. A small amount of matter can be seen forming a disk around the black hole. Time series of minimum lapse, maximum rest mass density, and

TABLE I. Physical properties of each EOS used in this study along with properties of NS near threshold. "Res." is the resolutions used for each EOS.

EOS	Res.	Gauge	k_{th}	C_{max}	$M_{g,max}$ ($M_\odot$)	C_{th}	Λ_{th}	$\Lambda_{1.4}$	$R_{1.4}$ (km)	$R_{1.6}$ (km)
SFHo	SR	IGD	1.37 ± 0.01	0.29	2.06	0.18 ± 0.01	312.94 ± 68.34	332.67	11.90	11.77
	LR		1.39 ± 0.01							
BHB	SR, LR	IGD	1.44 ± 0.01	0.27	2.10	0.17 ± 0.00	466.59 ± 50.89	754.43	13.22	13.21
SLy	SR, LR	IGD	1.36 ± 0.01	0.30	2.05	0.18 ± 0.00	314.40 ± 39.21	310.44	11.75	11.59
H4	SR, LR	IGD	1.52 ± 0.01	0.26	2.03	0.17 ± 0.00	487.06 ± 59.06	933.11	13.55	13.45
ALF2	SR, LR	IGD	1.48 ± 0.01	0.26	1.99	0.18 ± 0.00	436.98 ± 51.19	607.18	12.39	12.41
BLh	SR, LR	IGD	1.39 ± 0.01	0.30	2.10	0.17 ± 0.00	321.97 ± 36.59	430.29	12.42	12.24
		GD	1.39 ± 0.01							
BLQ	SR, LR	IGD	1.44 ± 0.01	0.28	1.99	0.17 ± 0.00	368.83 ± 40.64	434.57	12.40	12.23
		GD	1.43 ± 0.01							
SRO0	SR, LR	IGD	1.34 ± 0.01	0.30	2.21	0.18 ± 0.00	317.18 ± 33.55	433.19	12.33	12.26
SRO1	SR, LR	IGD	1.25 ± 0.01	0.32	2.30	0.18 ± 0.00	258.95 ± 27.60	309.37	11.67	11.64
SRO2	SR, LR	IGD	1.36 ± 0.01	0.29	2.16	0.17 ± 0.00	346.86 ± 36.99	474.57	12.51	12.45
SRO3	SR, LR	IGD	1.30 ± 0.01	0.31	2.23	0.18 ± 0.00	313.79 ± 32.87	393.73	11.96	11.96
SRO4	SR, LR	IGD	1.34 ± 0.01	0.30	2.20	0.17 ± 0.00	341.54 ± 37.01	478.06	12.53	12.41
SRO5	SR	IGD	1.31 ± 0.01	0.30	2.19	0.17 ± 0.01	400.08 ± 81.77	474.34	12.54	12.45
	LR		1.33 ± 0.01							
SRO6	SR	IGD	1.41 ± 0.01	0.27	2.11	0.17 ± 0.00	392.15 ± 62.18	589.98	12.87	12.82
	LR		1.44 ± 0.01							
SRO7	SR, LR	IGD	1.33 ± 0.01	0.31	2.22	0.18 ± 0.00	327.70 ± 35.91	463.74	12.36	12.28
SRO8	SR, LR	IGD	1.35 ± 0.01	0.30	2.18	0.17 ± 0.00	340.46 ± 38.82	473.99	12.71	12.55
LS220	SR, LR	IGD	1.45 ± 0.01	0.28	2.04	0.17 ± 0.00	377.03 ± 44.93	547.43	12.69	12.50
DD2	SR	IGD	1.35 ± 0.01	0.30	2.42	0.18 ± 0.01	300.42 ± 62.34	769.37	13.23	13.27
	LR		1.33 ± 0.01							
BA	SR	IGD	1.30 ± 0.03	0.31	2.60	0.19 ± 0.01	265.15 ± 63.33	739.03	13.04	13.18
	LR		1.32 ± 0.01							
GRW1	SR, LR	IGD	1.39 ± 0.01	0.29	2.39	0.19 ± 0.00	306.81 ± 28.41	818.98	13.07	13.20
GRW2	SR, LR	IGD	1.34 ± 0.01	0.30	2.38	0.19 ± 0.00	271.05 ± 25.40	553.33	12.26	12.40
H3	SR, LR	IGD	1.61 ± 0.01	0.22	1.70	0.15 ± 0.00	797.22 ± 117.74	655.56	13.06	12.48
DD2qG	SR	IGD	1.47 ± 0.01	0.25	2.15	0.18 ± 0.00	354.52 ± 30.51	690.24	13.27	13.29

gravitational wave strain for this binary can be found in the second column of Fig. 3.

The third row of Fig. 2 corresponds to a binary undergoing prompt collapse with a component mass of 1.5 $M_\odot$. The first panel, which shows the remnant ~1 ms after merger, indicates that the core has collapsed as the lapse has fallen below 0.2, at which point the two neutron stars are no longer distinguishable. The second frame sees the remnant shrink in size as more and more matter falls into the black hole or gets ejected. In the final frame, only the black hole remains with little to no trace of matter surrounding it. See the third column of Fig. 3 for quantities corresponding to this binary.

We calculate k_{th}, Λ_{th} and report them in Table I, along with properties of the NSs corresponding to the EOS used in our simulations.

A. Constraints on neutron star radii and maximum masses

Following the literature [18,21,26], we assume M_{th} for each EOS to be directly proportional to the maximum mass (M_{max}) for a nonrotating NS predicted by that EOS. Relations between M_{th}, M_{max} and C_{max} are given as

$$M_{th} = k_{th} M_{max}, \tag{1a}$$

$$k_{th} = aC_{max} + b, \tag{1b}$$

$$M_{th} = (aC_{max} + b) M_{max}, \tag{1c}$$

where a and b are coefficients of linear fits obtained using a weighted least-squares method. Rearranging the linear fit equation for k_{th} vs C_{max}, we obtain the following empirical relations:

$$R_{max} = \frac{G}{c^2}\left[\frac{aM_{max}^2}{M_{th} - bM_{max}}\right], \tag{2a}$$

$$M_{th} = \left[a\frac{GM_{max}}{R_{max}c^2} + b\right] M_{max}, \tag{2b}$$

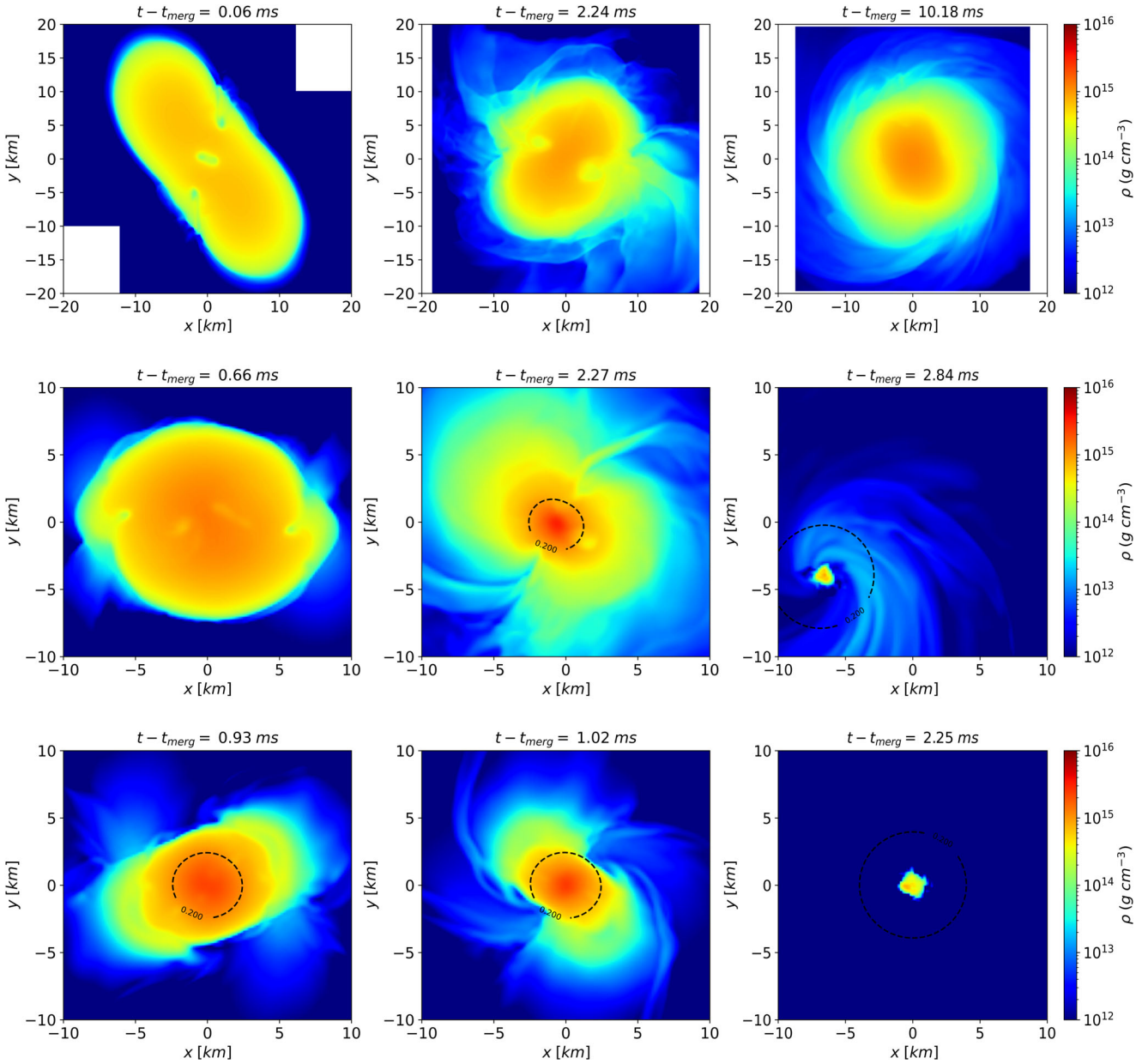

FIG. 2. Color map of rest mass density in two-dimensional slices taken along the equatorial plane of the binaries. The contour in some of the frames corresponds to lapse equals 0.2. Each row corresponds to slices from a different binary with individual masses, from top to bottom, 1.35 $M_\odot$, 1.45 $M_\odot$, and 1.5 $M_\odot$, respectively. Each binary is created using the EOS SRO2. In the middle row, the drift in the formed BH is a gauge effect and does not correspond to actual movement.

where a and b are fitting coefficients in Eq. (1b). We report these fits in Table II for our data, as well as various datasets in the literature. Using Eq. (2a), we plot the constant R_{max} contours in Fig. 4.

We find agreement with the claim that k_{th} is directly proportional to C_{max} and modified compactnesses $(C^*_{1.4}, C^*_{1.6})$, which are defined as follows:

$$C^*_{1.4} := \frac{GM_{max}}{c^2 R_{1.4}}, \tag{3a}$$

$$C^*_{1.6} := \frac{GM_{max}}{c^2 R_{1.6}}, \tag{3b}$$

where $R_{1.4}$ and $R_{1.6}$ are radii of a 1.4 $M_\odot$ and a 1.6 $M_\odot$ NS. We find the R-squared goodness of fit for $k_{th} - C_{max}$, $k_{th} - C^*_{1.6}$, and $k_{th} - C^*_{1.4}$ to be 0.93, 0.90, and 0.86, respectively. From the left panel of Fig. 4 and Table II, we can see that our data agree closely with that of Hotokezaka *et al.* [11], who use an independent $3+1$ numerical relativity implementation for solving Einstein's equations. On the other hand, we see a systematic deviation from the results of

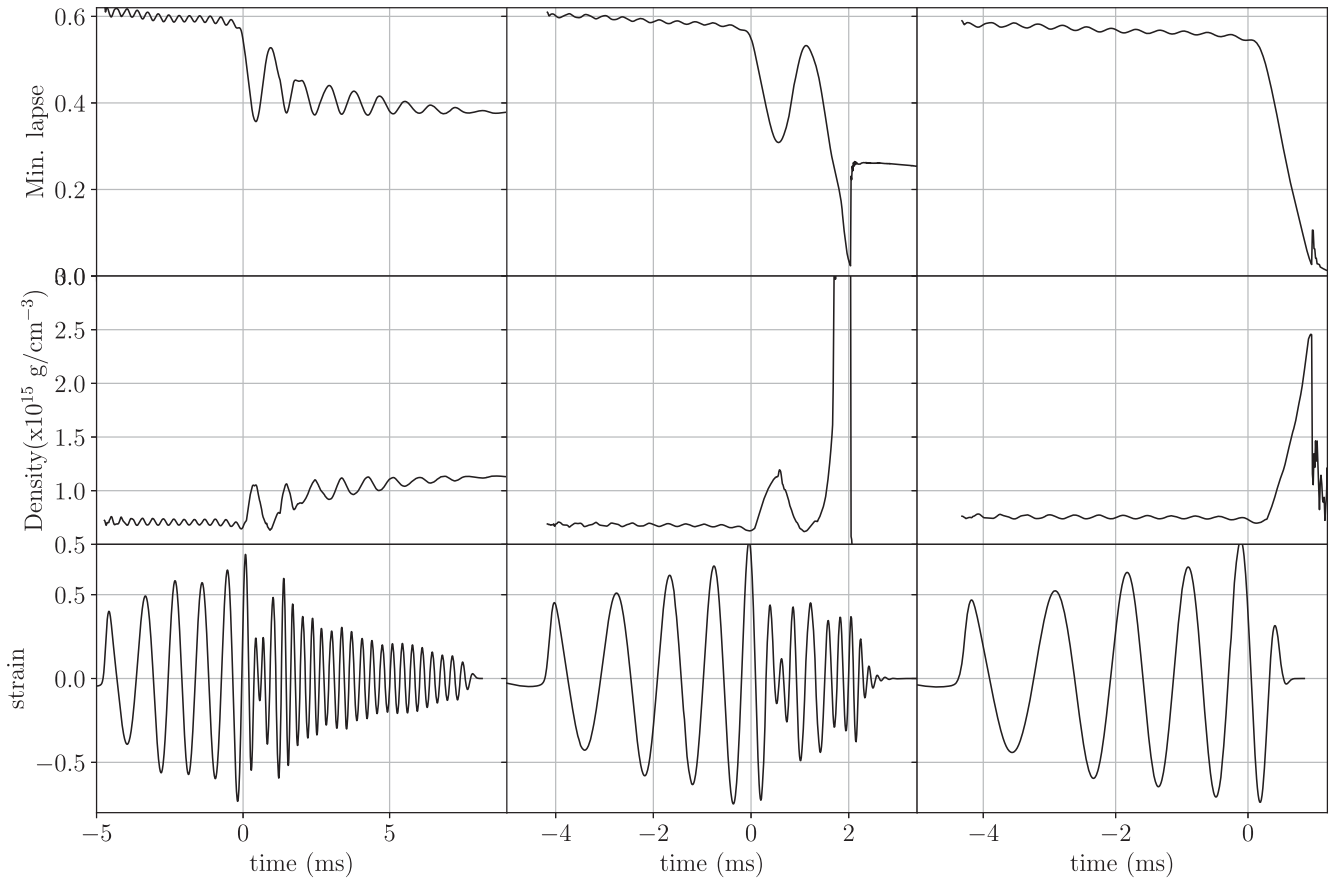

FIG. 3. Examples of the minimum lapse function, maximum rest mass densities, and $l = 2$, $m = 2$ mode gravitational wave strains (in geometric units of total mass of binaries) from three different simulations (from left to right: EOS2-1.36 $M_\odot$, EOS6-1.48 $M_\odot$, and EOS2-1.51 $M_\odot$ binary systems). The first column shows a binary resulting in a massive neutron star that does not collapse during the simulation. The binary in the second column produces a massive neutron star that rapidly collapses to a black hole after a single core bounce. The binary shown in the third column collapses immediately upon merger and is classified as prompt collapse.

Bauswein *et al.* [18], who uses an implementation of conformally flat approximation. However, the improved version of their viscosity treatment gives consistent results with our fitting coefficients [22].

Using the linear correlation between k_{th} and C_{max} discussed above and the phenomenological constraints on the absolute maximum value of C_{max}, it is possible to derive a lower bound for R_{max} [20,26]. We recompute this constraint using our fit of k_{th} vs C_{max}.

Independent phenomenological constraints on upper and lower limits of R_{max} have also been obtained using our data [31,73,74], which depend on the maximum masses in the range 1.97 $M_\odot$–2.9 $M_\odot$ as shown in Fig. 9. We use two million piecewise polytropic (PWP) EOS to construct the key properties such as mass, radius, and tidal deformability of 1.4 $M_\odot$, 1.6 $M_\odot$, and maximum mass NSs (see the Appendix for details). Our data show the maximum value of M_{max} to be 2.9 $M_\odot$ which rules out the region to the right of this value in Fig. 4. The minimum value of M_{max} is determined by the maximum mass pulsar observed until date (~2.01 $M_\odot$), which excludes the region to the left of it. We use Eq. (2b) to calculate the limits of M_{th} at each value of M_{max} corresponding to minimum and maximum values of R_{max} taken from Fig. 9. The computed threshold mass limits (corresponding to R_{max} limits) are plotted as dot-dashed black lines on the right panel in Fig. 4, ruling out the region above the upper and below the lower line. The horizontal line corresponding to the mass of GW170817 rules out the region below it due to its identification as a delayed collapse event. The contour of constant R_{max} passing through the lowest point of the unshaded region provides the minimum allowed value of R_{max} (see Fig. 4).

Similarly, using our data of simulated PWP EOS, we also plot the M_{max}-dependent minimum and maximum values of $R_{1.4}$ and $R_{1.6}$ as shown in Figs. 10 and 11. We define linear relations between k_{th} and the modified compactness parameters $C^*_{1.6}$ and $C^*_{1.4}$ similar to Eq. (1b). We obtain expressions for $R_{1.4}$ and $R_{1.6}$ similar to Eq. (2a), as well as for M_{th} as a function of $R_{1.4}$ and $R_{1.6}$ similar to Eq. (2b). Our newly found correlation between k_{th} and modified

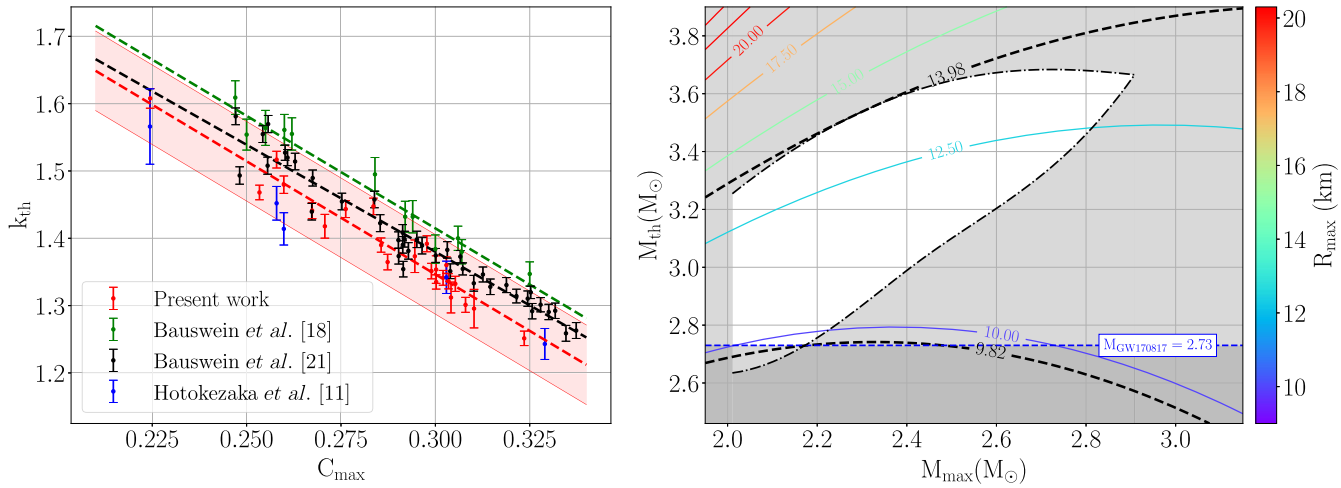

FIG. 4. Left: plot of k_{th} vs C_{max} from present and previous works [11,18,22]. Fits are constructed using our data and are shown in combination with the data of Hotokezaka *et al.* [11] and Bauswein *et al.* [18,22]. The weighted linear regression results take into account the uncertainty in k_{th}. The shaded region represents uncertainties in the intercept. Right: constraints on the R_{max}, M_{max}, and M_{th} obtained using the correlation on the left, PWP phenomenological constraints in combination with the observational lower limit on the maximum mass of nonrotating neutron stars, and total mass of the event GW170817 as the lowest limit for prompt collapse.

compactness $C^*_{1.4}$ (see Fig. 6) provides a constraint on $R_{1.4}$, which is a known constraining factor for pressure at 2 times saturation density [75].

The same procedure as described above is used to plot contours of constant $R_{1.6}$ in Fig. 5 and of constant $R_{1.4}$ in Fig. 6. Constraints for $R_{1.6}$ and $R_{1.4}$ and excluded regions for M_{th} and M_{max} are obtained analogous to R_{max} as shown in Figs. 5 and 6, respectively. We report the constraints on minimum values of $R_{1.6}$ and $R_{1.4}$ in Table II with the uncertainty that takes into account the uncertainties in the mass of GW170817 as well as our derived value of intercepts for the linear fits.

Extending the method from the previous works [21,22,26], we find that the constraints on the threshold masses as shown in the figures above provide a method to constrain the lower and upper limits on the maximum mass of nonrotating NS as follows. Because of the lower (upper) limit on R_{max}, we obtain a lower (upper) limit on M_{th} for a given value of M_{max} using Eq. (2b) as shown in Fig. 4. The dependence of M_{th} bounds on M_{max} implies constraints on the maximum mass of NS if we infer an unambiguous prompt collapse or delayed collapse in a future BNS detection. This is so because observation of a prompt collapse event with total mass ($M_{total,Prompt}$) less than 3.64 $M_\odot$ (Table III) will exclude the region above the horizontal line corresponding to that mass. If observed in future GW detections, and with M_{total} greater than this value, we will obtain a constraint on the upper bound of maximum mass better than the one obtained using PWP phenomenological constraints ($\approx$2.9 $M_\odot$). The constraining upper value of maximum mass will be the intersection point of the horizontal line at $M_{total,Prompt}$ and the upper bounding curve of M_{th} in Fig. 4. One can also deduce another constraining fact from these figures that, if we observe an event with delayed collapse, like GW170817, with total mass ($M_{total,Delayed}$) greater than 3.25 $M_\odot$, we can constrain the lower limit of maximum masses better than the current best estimate from pulsar

TABLE II. Fitting coefficients in Eq. (1b) and radius constraints obtained from our data as well as from literature. The fitting coefficients and their uncertainties are reported using a weighted least-squares method. The uncertainties in radii comes from the uncertainties in the mass of GW170817 as well as in the values of fitting coefficients. Please note that the upper limits on radii are purely PWP phenomenological constraints.

Dataset	a	b	min(R_{max}) (km)	max(R_{max}) (km)	min($R_{1.6}$) (km)	max($R_{1.6}$) (km)	min($R_{1.4}$) (km)	max($R_{1.4}$) (km)
Bauswein *et al.* [18]	−3.342	2.42	⋯	⋯	⋯	⋯	⋯	⋯
Bauswein *et al.* [26]	−3.38	2.43	$9.26^{+0.17}_{-0.03}$	$10.30^{+0.15}_{-0.03}$	⋯	⋯	⋯	⋯
Current work	-3.36 ± 0.20	2.35 ± 0.06	$9.81^{+1.20}_{-1.09}$	13.98	$10.90^{+1.85}_{-1.42}$	13.72	$10.74^{+1.86}_{-1.61}$	13.87

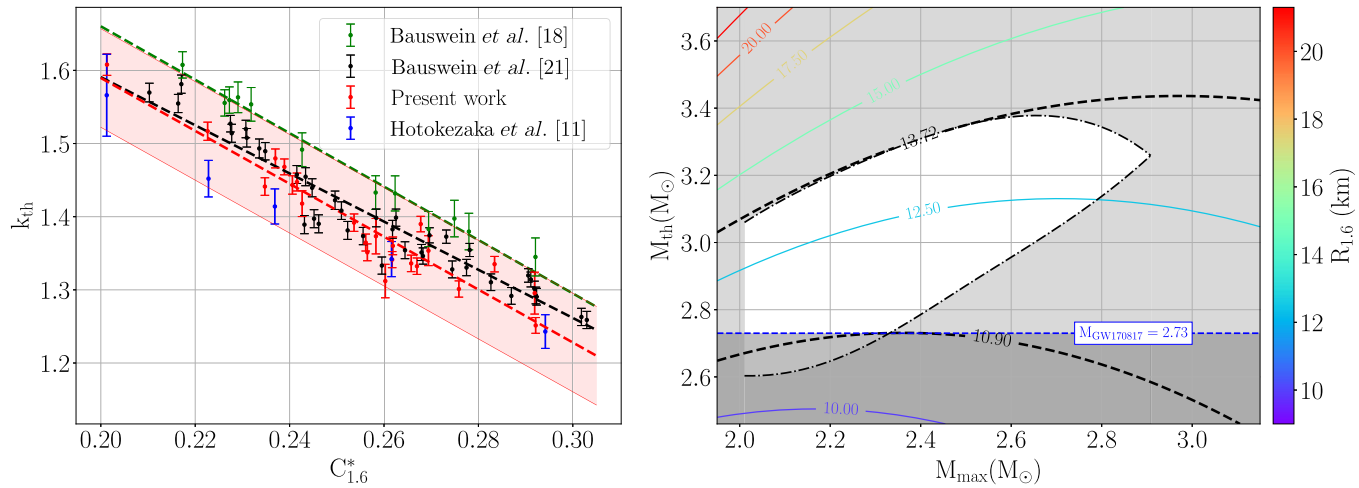

FIG. 5. Left: plot of k_{th} vs $C^*_{1.6}$ from present and previous works [11,18,22]. Fits are constructed using our data and are shown in combination with the data of Hotokezaka *et al.* [11] and Bauswein *et al.* [18,22]. The weighted linear regression results take into account the uncertainty in k_{th}. The shaded region represents uncertainties in the intercept. Right: Constraints on the $R_{1.6}$, M_{max}, and M_{th} obtained using the correlation on the left, PWP phenomenological constraints obtained using the correlation on the left, PWP phenomenological constraints in combination with the observational lower limit on the maximum mass of nonrotating neutron stars, and total mass of the event GW170817 as the lowest limit for prompt collapse.

observations. The constraint on the lower limit of the maximum mass will be the intersection point of the horizontal line corresponding to $M_{total,Delayed}$ and the lower bounding curve of M_{th} in Fig. 4.

The lower and upper constraints on M_{max} as well as maximum value of threshold masses corresponding to the correlations of $k_{th} - C^*_{1.6}$ and $k_{th} - C^*_{1.4}$ can be obtained using a similar procedure. The critical values of $M_{total,Prompt}$ and $M_{total,Delayed}$ from corresponding correlations as shown in Figs. 4–6 are quoted in Table III.

B. Implications on tidal deformability

Following Bauswein *et al.* [21], we fit the threshold mass as a bilinear function of M_{max} and the tidal deformability of the 1.4 $M_\odot$ NS ($\Lambda_{1.4}$),

$$M_{th}(\Lambda_{1.4}, M_{max}) = s_0 M_{max} + s_2 \Lambda_{1.4} + s_3, \qquad (4)$$

where the fitting coefficients obtained using our data are $s_0 = 0.62 \pm 0.05$, $s_1 = (5.83 \pm 0.56) \times 10^{-4}$, and $s_3 = 1.33 \pm 0.11$. We propose to combine the approach of

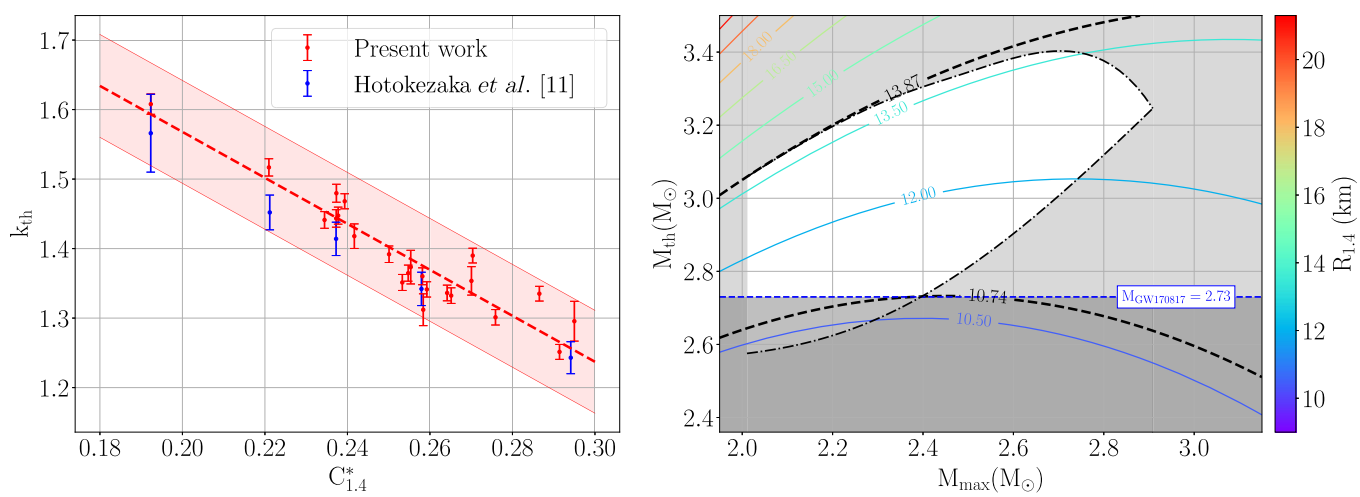

FIG. 6. Left: plot of k_{th} vs $C^*_{1.4}$ from present and previous works [11]. Fits are constructed using our data in combination with the data of Hotokezaka *et al.* [11]. The weighted linear regression results take into account the uncertainty in k_{th}. The shaded region represents uncertainties in the intercept. Right: constraints on the $R_{1.4}$, M_{max}, and M_{th} obtained using the correlation on the left, PWP phenomenological constraints obtained using the correlation on the left, PWP phenomenological constraints in combination with the observational lower limit on the maximum mass of nonrotating neutron stars, and total mass of the event GW170817 as the lowest limit for prompt collapse.

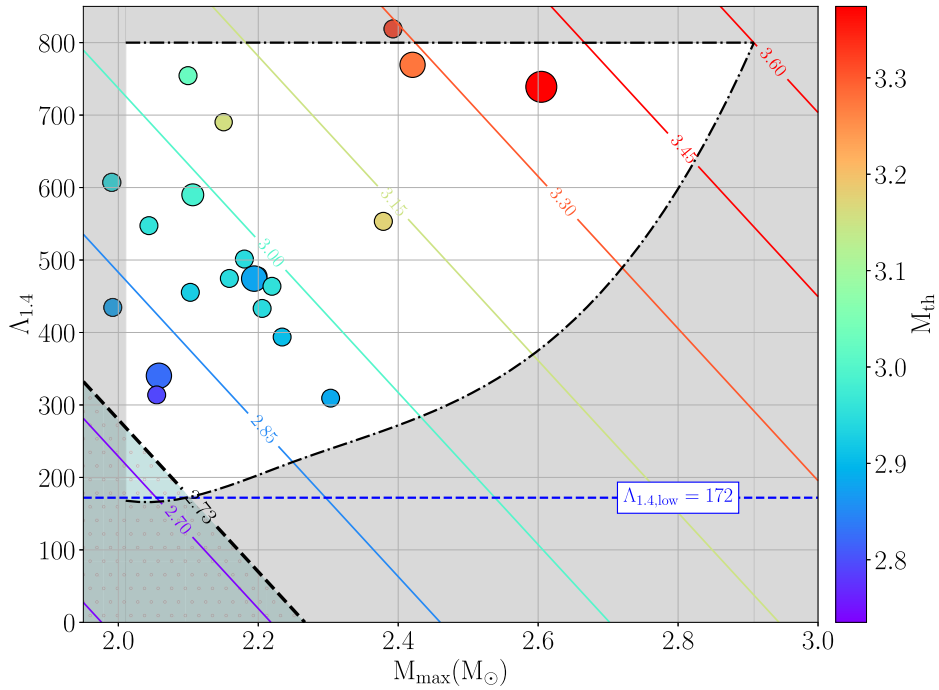

FIG. 7. Data (colored circles) and linear relationships obtained from the fit in Eq. (4) relating M_{th} to M_{max} and $\Lambda_{1.4}$ (solid contour lines). Black dot-dashed curves shows the most conservative upper and lower constraint on $\Lambda_{1.4}$ from [31] (see also values in [1] 190^{+390}_{-120}). Please note the two contours in thick dashed black lines: for 2.73 $M_\odot$ corresponding to the total mass of GW170817 ($M = 2.73^{+0.04}_{-0.01}$, [1]) and for the maximum threshold mass to be equal to 3.62 $M_\odot$. We report the upper limit of threshold mass below which we can constrain the upper limit of NS maximum mass.

Bauswein *et al.* [21] along with PWP constraints to find the lower limit of $\Lambda_{1.4}$ as follows. In addition to the data points (as colored circles) and contours of the constant M_{th}, we plot several observational and phenomenological constraints in Fig. 7. The lower limit of NS maximum mass from pulsar observation ($M_{max} > 2.01\ M_\odot$) excludes the region left of this value, while the upper limit of $\Lambda_{1.4}$ from the observation of GW170817 ($\Lambda_{1.4} < 800$) eliminates the region above the horizontal line corresponding to this value. We again use our PWP phenomenological data to plot M_{max}-dependent constraint on the lower limit of $\Lambda_{1.4}$ (lower dot-dashed black curve in Fig. 7), ruling out the region below this curve. The lowest point of the allowed (unshaded) region gives the lower limit on $\Lambda_{1.4}$ ($= 172$), which corresponds to the intersection point of the slanted line corresponding to $M_{th} = 2.73\ M_{odot}$ (total mass of GW170817) and the lower bounding curve of $\Lambda_{1.4}$.

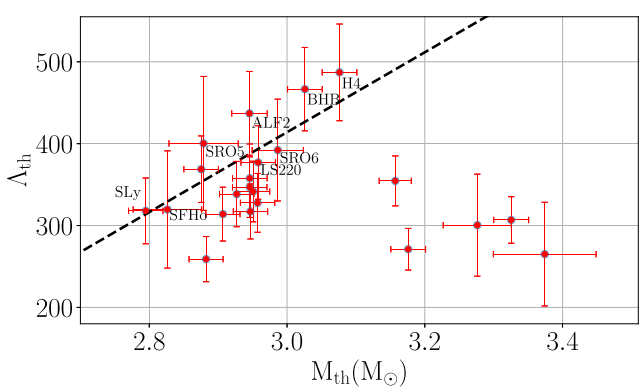

FIG. 8. Plot of Λ_{th} vs M_{th}. We find one nucleonic (SRO5) and two non-nucleonic EOS (BHB, H4) whose values lie in the forbidden zone (above dashed black line as proposed by [22]) for nucleonic EOS, but with their error bars extending below the critical line. There are few other EOS such as SFHo, SLy, SRO6, and LS220 whose values lie below the critical line, but with error bars extending above it. The EOS H3 lies above the critical line and outside the plot, which we have removed for clarity.

We also report the distribution of our data points on the Λ_{th}-M_{th} plane where Λ_{th} is the tidal deformability of a NS with mass equal to half of M_{th} (see Fig. 8). In agreement with Bauswein *et al.* [22], we find that most of our nucleonic EOS lie below the critical line in this plane. However, we find that data points of one nucleonic (SRO5) and two non-nucleonic EOS (BHB, H4) lie in the forbidden region, with their error bars extending below the critical line. Similarly, error bars of some nucleonic EOS that lie below the critical line extend above it; these are SFHo, SLy, SRO6, and LS220. Further high resolution runs are required to resolve these issues and to correctly assess their claim.

V. CONCLUSIONS AND DISCUSSIONS

In this work, we present a survey of binary neutron star merger outcomes for 23 different EOS models with various assumptions about the nuclear matter. We perform

numerical relativity simulations of equal-mass binary NS coalescences with varying total masses and classify the outcomes as either prompt or delayed collapse. We confirm the correlations claimed in the literature and report different correlation coefficients for k_{th}-C^*_{max} and k_{th}-$C^*_{1.6}$ [18,26], although similar to Bauswein *et al.* [22]. The linear fit reported in Bauswein *et al.* [18,26] lies outside the error bars obtained in our analysis, but their updated results are more consistent with ours [22]. With the use of numerical relativity and careful error considerations, our fitting coefficients will be best suited for any future applications of this work. We have discovered a new correlation for k_{th}-$C^*_{1.4}$, allowing us to put a lower bound on $R_{1.4}$. We find better bounds on R_{max} (≥ 9.81 km) and $R_{1.6}$ (≥ 10.90 km) taking into account uncertainties in the fitting coefficients and the mass of GW170817. These values are in agreement with those found by Köppel *et al.* [20] ($R_{1.4} \geq 9.74$ km and $R_{1.6} \geq 10.90$ km).

Most importantly, we introduce an M_{max}-dependent condition on both upper and lower limits of compactness (equivalently radius) ($C_{max}, C^*_{1.4}, C^*_{1.6}$) to derive constraints on upper and lower limits of M_{max}. This improves upon previous methods by Bauswein *et al.* [26] where they use only the absolute maximum limit on compactness. We also use lower limits on compactness, not used earlier, which allows us to put novel constraints on both the upper limit of M_{th} as well as the lower limit of M_{max}. Such critical values of total masses corresponding to different correlations allow us to put bounds on M_{max} as reported in Table III. In addition, we also find the lower limit on $\Lambda_{1.4}$ to be 172 deduced from the bilinear fit of M_{th} as a function of M_{max} and $\Lambda_{1.4}$ and constraints from GW170817 (see Fig. 7). We emphasize that the phenomenological constraints on R_{max}, $R_{1.4}$, and $R_{1.6}$ are obtained using the formulation of EOS as a piecewise polytropic pressure-density curve and hence inherit its limitations.

We demonstrate that the method discussed here to derive lower and upper constraints can be applied to future GW observations and their identification as delayed and prompt collapse, respectively. GW detectors are being planned to higher sensitivity, which will increase the detection range as well as the accuracy of the measurements, most notably of the total masses. In future GW detectors, it will be possible to determine the likelihood of a prompt or delayed collapse following the merger using the presence or absence, respectively, of a sharp cutoff in the GW from a BNS event along with a lack of kilonova observation. Such estimate will introduce horizontal lines on Figs. 4–6, ruling out regions above or below them for a prompt or a delayed collapse, respectively. In the era of highly sensitive GW observatories, tens of thousands of BNS event are expected to be detected. We are hopeful that the methodology presented here will put a strong constraint on the maximum masses and hence on the EOS of the nuclear matter. We note the limitations in our work due to unexplored regions of BNS parameter space due to neglected effect such as spin of component NSs. We intend to extend and improve our study in a future work.

TABLE III. Critical values of total binary masses for future GW observations for the present methods to put constraints on M_{max}. Note that the current minimum threshold mass for prompt collapse is set by $M_{GW170817} = 2.73$. We report the total binary masses above which a potential delayed collapse will constrain the minimum value of M_{max}, as well as total masses below which a future prompt collapse event will constrain the maximum value of M_{max}.

Correlation	$\max(M_{th})$ ($M_\odot$)	$M_{total,\mathbf{Delayed}}$ to constrain $\min(M_{max})$ ($M_\odot$)	$M_{total,\mathbf{Prompt}}$ to constrain $\max(M_{max})$ ($M_\odot$)
k_{th}-C_{max}	3.67	>3.25	<3.64
k_{th}-$C^*_{1.4}$	3.38	>3.05	<3.20
k_{th}-$C^*_{1.6}$	3.35	>3.05	<3.22
M_{th}-$(\Lambda_{1.4}M_{max})$	3.62	...	...

ACKNOWLEDGMENTS

This research was funded by U.S. Department of Energy, Office of Science, Division of Nuclear Physics under Award No. DE-SC0021177 and by the National Science Foundation under Grants No. PHY-2011725, No. PHY-2020275, No. PHY-2116686, and No. AST-2108467. S. B. acknowledges support by the EU H2020 under ERC Starting Grant No. BinGraSp-714626. NR simulations were performed on Bridges, Comet, Stampede2 (NSF XSEDE allocation TG-PHY160025), and NSF/NCSA Blue Waters (NSF AWD-1811236) supercomputers. Computations for this research were also performed on the Pennsylvania State University's Institute for Computational and Data Sciences' Roar supercomputer. This research used resources of the National Energy Research Scientific Computing Center, a DOE Office of Science User Facility supported by the Office of Science of the U.S. Department of Energy under Contract No. DE-AC02-05CH11231. Computations were also performed on the supercomputer SuperMUC-NG at the Leibniz-Rechenzentrum Munich and on the national HPE Apollo Hawk at the High Performance Computing Center Stuttgart (HLRS). The authors acknowledge the Gauss Centre for Supercomputing e.V. (www.gauss-centre.eu) for funding this project by providing computing time to the GCS Supercomputer SuperMUC-NG at LRZ (allocation pn68wi). The authors acknowledge HLRS for funding this project by providing access to the supercomputer HPE Apollo Hawk under the Grant No. INTRHYGUE/44215. Finally, computations were also performed on the supercomputer Joliot-Curie at GENCI@CEA and A. Perego acknowledge PRACE for awarding him access to Joliot-Curie at GENCI@CEA (PRACE Project: 2019215202).

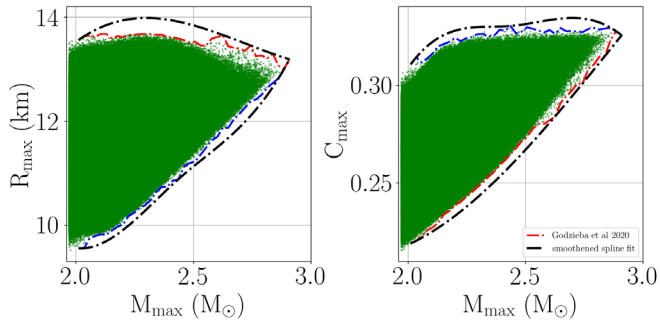

FIG. 9. Maximum and minimum compactness and corresponding radii of maximum mass NS as a function of maximum mass. The dashed black line represents a conservative bound, while the red and blue dashed lines represent the actual limit of the dataset.

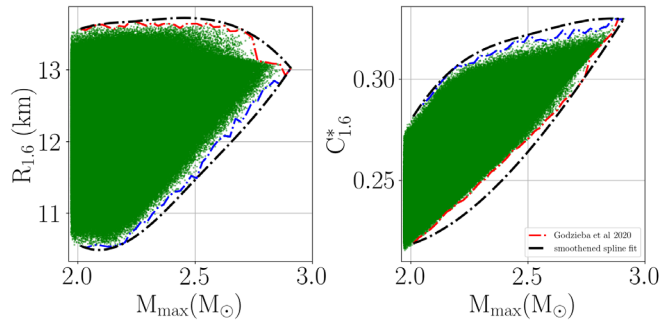

FIG. 10. Maximum and minimum modified compactness [$C^*_{1.6}$, Eq. (3b)] and corresponding radii of a 1.6 $M_\odot$ NS as a function of maximum mass. The dashed black line represents a conservative bound, while the red and blue dashed lines represent the actual limit of the dataset.

APPENDIX: RESULTS USING DATA FROM [31]

We use data from about two million piecewise polytropic EOS satisfying causality, along with some other important constraints mentioned in [31], to obtain the phenomenological upper and lower limits on compactness of nonrotating NSs. We find that for any given maximum mass there exists an upper and lower limit on C_{max}, $C^*_{1.6}$, and $C^*_{1.4}$ as shown in Figs. 9–11. We construct bins in the array of maximum masses and select the minimum and maximum values of radii corresponding to maximum mass, as well of 1.4 $M_\odot$ and 1.6 $M_\odot$ NSs.

We use a conservative limit from the dataset by constructing a smoothened spline fit with few points. We transform the bounds on radii to the bounds on threshold masses depending upon maximum mass of the NS using Eq. (2b) plotted in Fig. 4.

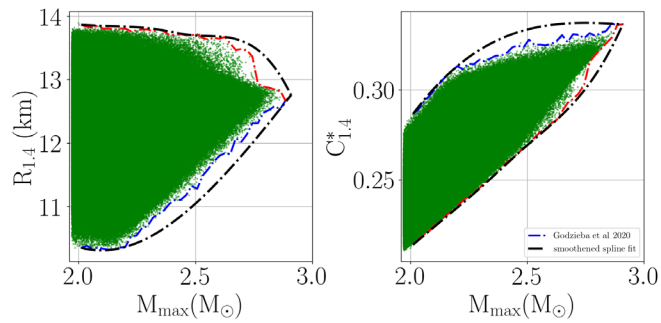

FIG. 11. Maximum and minimum modified compactness [$C^*_{1.4}$, Eq. (3a)] and corresponding radii of a 1.4 $M_\odot$ NS as a function of maximum mass. The dashed black line represents a conservative bound, while the red and blue dashed lines represent the actual limit of the dataset.

[1] B. P. Abbott *et al.* (LIGO Scientific, Virgo Collaborations), GW170817: Observation of Gravitational Waves from a Binary Neutron Star Inspiral, Phys. Rev. Lett. **119**, 161101 (2017).

[2] B. P. Abbott *et al.* (LIGO Scientific, Virgo Collaborations), GW190425: Observation of a compact binary coalescence with total mass ~3.4 $M_\odot$, Astrophys. J. Lett. **892**, L3 (2020).

[3] L.-X. Li and B. Paczyński, Transient events from neutron star mergers, Astrophys. J. **507**, L59 (1998).

[4] S. Kulkarni, Modeling supernova-like explosions associated with gamma-ray bursts with short durations, arXiv:astro-ph/0510256.

[5] B. Metzger, G. Martinez-Pinedo, S. Darbha, E. Quataert, A. Arcones, D. Kasen, R. Thomas, P. Nugent, I. V. Panov, and N. T. Zinner, Electromagnetic counterparts of compact object mergers powered by the radioactive decay of R-process nuclei, Mon. Not. R. Astron. Soc. **406**, 2650 (2010).

[6] D. Kasen, N. Badnell, and J. Barnes, Opacities and spectra of the r-process ejecta from neutron star mergers, Astrophys. J. **774**, 25 (2013).

[7] M. Tanaka and K. Hotokezaka, Radiative transfer simulations of neutron star merger ejecta, Astrophys. J. **775**, 113 (2013).

[8] B. D. Metzger, Kilonovae, Living Rev. Relativity **23**, 1 (2020).

[9] K. Hotokezaka, M. Tanaka *et al.*, Nebular emission from lanthanide-rich ejecta of neutron star merger, Mon. Not. R. Astron. Soc. **506**, 5863 (2021).

[10] M. Shibata, K. Taniguchi, and K. Uryū, Merger of binary neutron stars with realistic equations of state in full general relativity, Phys. Rev. D **71**, 084021 (2005).

[11] K. Hotokezaka, K. Kyutoku, H. Okawa, M. Shibata, and K. Kiuchi, Binary neutron star mergers: Dependence on the nuclear equation of state, Phys. Rev. D **83**, 124008 (2011).

[12] K. Hotokezaka, K. Kiuchi, K. Kyutoku, H. Okawa, Y.-I. Sekiguchi, M. Shibata, and K. Taniguchi, Mass ejection

from the merger of binary neutron stars, Phys. Rev. D **87**, 024001 (2013).

[13] A. Bauswein, S. Goriely, and H. T. Janka, Systematics of dynamical mass ejection, nucleosynthesis, and radioactively powered electromagnetic signals from neutron-star mergers, Astrophys. J. **773**, 78 (2013).

[14] D. Radice, A. Perego, F. Zappa, and S. Bernuzzi, GW170817: Joint constraint on the neutron star equation of state from multimessenger observations, Astrophys. J. Lett. **852**, L29 (2018).

[15] D. Radice, A. Perego, K. Hotokezaka, S. A. Fromm, S. Bernuzzi, and L. F. Roberts, Binary neutron star mergers: Mass ejection, electromagnetic counterparts and nucleosynthesis, Astrophys. J. **869**, 130 (2018).

[16] K. Kiuchi, K. Kyutoku, M. Shibata, and K. Taniguchi, Revisiting the lower bound on tidal deformability derived by AT 2017gfo, Astrophys. J. Lett. **876**, L31 (2019).

[17] S. Bernuzzi *et al.*, Accretion-induced prompt black hole formation in asymmetric neutron star mergers, dynamical ejecta and kilonova signals, Mon. Not. R. Astron. Soc. **497**, 1488 (2020).

[18] A. Bauswein, T. W. Baumgarte, and H. T. Janka, Prompt Merger Collapse and the Maximum Mass of Neutron Stars, Phys. Rev. Lett. **111**, 131101 (2013).

[19] F. Zappa, S. Bernuzzi, D. Radice, A. Perego, and T. Dietrich, Gravitational-Wave Luminosity of Binary Neutron Stars Mergers, Phys. Rev. Lett. **120**, 111101 (2018).

[20] S. Köppel, L. Bovard, and L. Rezzolla, A general-relativistic determination of the threshold mass to prompt collapse in binary neutron star mergers, Astrophys. J. Lett. **872**, L16 (2019).

[21] A. Bauswein, S. Blacker, V. Vijayan, N. Stergioulas, K. Chatziioannou, J. A. Clark, N.-U. F. Bastian, D. B. Blaschke, M. Cierniak, and T. Fischer, Equation of State Constraints from the Threshold Binary Mass for Prompt Collapse of Neutron Star Mergers, Phys. Rev. Lett. **125**, 141103 (2020).

[22] A. Bauswein, S. Blacker, G. Lioutas, T. Soultanis, V. Vijayan, and N. Stergioulas, Systematics of prompt black-hole formation in neutron star mergers, Phys. Rev. D **103**, 123004 (2021).

[23] T. Damour, A. Nagar, and L. Villain, Measurability of the tidal polarizability of neutron stars in late-inspiral gravitational-wave signals, Phys. Rev. D **85**, 123007 (2012).

[24] B. P. Abbott *et al.* (LIGO Scientific, Virgo, Fermi GBM, INTEGRAL, IceCube, AstroSat Cadmium Zinc Telluride Imager Team, IPN, Insight-Hxmt, ANTARES, Swift, AGILE Team, 1M2H Team, Dark Energy Camera GW-EM, DES, DLT40, GRAWITA, Fermi-LAT, ATCA, ASKAP, Las Cumbres Observatory Group, OzGrav, DWF (Deeper Wider Faster Program), AST3, CAASTRO, VINROUGE, MASTER, J-GEM, GROWTH, JAGWAR, CaltechNRAO, TTU-NRAO, NuSTAR, Pan-STARRS, MAXI Team, TZAC Consortium, KU, Nordic Optical Telescope, ePESSTO, GROND, Texas Tech University, SALT Group, TOROS, BOOTES, MWA, CALET, IKI-GW Follow-up, H.E.S.S., LOFAR, LWA, HAWC, Pierre Auger, ALMA, Euro VLBI Team, Pi of Sky, Chandra Team at McGill University, DFN, ATLAS Telescopes, High Time Resolution Universe Survey, RIMAS, RATIR, SKA South Africa/MeerKAT Collaborations), Multi-messenger observations of a binary neutron star merger, Astrophys. J. Lett. **848**, L12 (2017).

[25] B. Margalit and B. D. Metzger, Constraining the maximum mass of neutron stars from multi-messenger observations of GW170817, Astrophys. J. Lett. **850**, L19 (2017).

[26] A. Bauswein, O. Just, H.-T. Janka, and N. Stergioulas, Neutron-star radius constraints from GW170817 and future detections, Astrophys. J. Lett. **850**, L34 (2017).

[27] S. D. Tootle, L. Jens Papenfort, E. R. Most, and L. Rezzolla, Quasi-universal behaviour of the threshold mass in unequal-mass, spinning binary neutron-star mergers, Astrophys. J. Lett. **922**, L19 (2021).

[28] M. Agathos, F. Zappa, S. Bernuzzi, A. Perego, M. Breschi, and D. Radice, Inferring prompt black-hole formation in neutron star mergers from gravitational-wave data, Phys. Rev. D **101**, 044006 (2020).

[29] A. Perego, D. Logoteta, D. Radice, S. Bernuzzi, R. Kashyap, A. Das, S. Padamata, and A. Prakash, Probing the incompressibility of nuclear matter at ultra-high density through the prompt collapse of asymmetric neutron star binaries, arXiv:2112.05864.

[30] M. Kölsch, T. Dietrich, M. Ujevic, and B. Bruegmann, Investigating the mass-ratio dependence of the prompt-collapse threshold with numerical-relativity simulations (2021).

[31] D. A. Godzieba, R. Gamba, D. Radice, and S. Bernuzzi, Updated universal relations for tidal deformabilities of neutron stars from phenomenological equations of state, Phys. Rev. D **103**, 063036 (2021).

[32] I. Bombaci and D. Logoteta, Equation of state of dense nuclear matter and neutron star structure from nuclear chiral interactions, Astron. Astrophys. **609**, A128 (2018).

[33] D. Logoteta, A. Perego, and I. Bombaci, Microscopic equation of state of hot nuclear matter for numerical relativity simulations, Astron. Astrophys. **646**, A55 (2021).

[34] S. Typel, G. Ropke, T. Klahn, D. Blaschke, and H. H. Wolter, Composition and thermodynamics of nuclear matter with light clusters, Phys. Rev. C **81**, 015803 (2010).

[35] M. Hempel and J. Schaffner-Bielich, Statistical model for a complete supernova equation of state, Nucl. Phys. **A837**, 210 (2010).

[36] J. M. Lattimer and F. D. Swesty, A generalized equation of state for hot, dense matter, Nucl. Phys. **A535**, 331 (1991).

[37] A. W. Steiner, M. Hempel, and T. Fischer, Core-collapse supernova equations of state based on neutron star observations, Astrophys. J. **774**, 17 (2013).

[38] F. Douchin and P. Haensel, A unified equation of state of dense matter and neutron star structure, Astron. Astrophys. **380**, 151 (2001).

[39] A. S. Schneider, L. F. Roberts, and C. D. Ott, Open-source nuclear equation of state framework based on the liquid-drop model with Skyrme interaction, Phys. Rev. C **96**, 065802 (2017).

[40] A. S. Schneider, L. F. Roberts, C. D. Ott, and E. O'connor, Equation of state effects in the core collapse of a 20-$M_\odot$ star, Phys. Rev. C **100**, 055802 (2019).

[41] F. J. Fattoyev, C. J. Horowitz, J. Piekarewicz, and B. Reed, GW190814: Impact of a 2.6 solar mass neutron star on the

nucleonic equations of state, Phys. Rev. C **102**, 065805 (2020).

[42] S. Banik, M. Hempel, and D. Bandyopadhyay, New hyperon equations of state for supernovae and neutron stars in density-dependent hadron field theory, Astrophys. J. Suppl. Ser. **214**, 22 (2014).

[43] N. K. Glendenning and S. A. Moszkowski, Reconciliation of Neutron Star Masses and Binding of the Lambda in Hypernuclei, Phys. Rev. Lett. **67**, 2414 (1991).

[44] B. D. Lackey, M. Nayyar, and B. J. Owen, Observational constraints on hyperons in neutron stars, Phys. Rev. D **73**, 024021 (2006).

[45] J. S. Read, B. D. Lackey, B. J. Owen, and J. L. Friedman, Constraints on a phenomenologically parametrized neutron-star equation of state, Phys. Rev. D **79**, 124032 (2009).

[46] A. Prakash, D. Radice, D. Logoteta, A. Perego, V. Nedora, I. Bombaci, R. Kashyap, S. Bernuzzi, and A. Endrizzi, Signatures of deconfined quark phases in binary neutron star mergers, Phys. Rev. D **104**, 083029 (2021).

[47] D. Logoteta, I. Bombaci, and A. Perego, Isoentropic equations of state of β-stable hadronic matter with a quark phase transition, Eur. Phys. J. A **58**, 55 (2022).

[48] M. Alford, M. Braby, M. W. Paris, and S. Reddy, Hybrid stars that masquerade as neutron stars, Astrophys. J. **629**, 969 (2005).

[49] E. S. Fraga, R. D. Pisarski, and J. Schaffner-Bielich, Small, dense quark stars from perturbative QCD, Phys. Rev. D **63**, 121702 (2001).

[50] M. Alford, M. Braby, M. Paris, and S. Reddy, Hybrid stars that masquerade as neutron stars, Astrophys. J. **629**, 969 (2005).

[51] S. Weissenborn, I. Sagert, G. Pagliara, M. Hempel, and J. Schaffner-Bielich, Quark matter in massive compact stars, Astrophys. J. Lett. **740**, L14 (2011).

[52] N. K. Glendenning, First order phase transitions with more than one conserved charge: Consequences for neutron stars, Phys. Rev. D **46**, 1274 (1992).

[53] A. Bauswein, H. T. Janka, and R. Oechslin, Testing approximations of thermal effects in neutron star merger simulations, Phys. Rev. D **82**, 084043 (2010).

[54] A. Endrizzi, D. Logoteta, B. Giacomazzo, I. Bombaci, W. Kastaun, and R. Ciolfi, Effects of chiral effective field theory equation of state on binary neutron star mergers, Phys. Rev. D **98**, 043015 (2018).

[55] A. Figura, J. J. Lu, G. F. Burgio, Z. H. Li, and H. J. Schulze, Hybrid equation of state approach in binary neutron-star merger simulations, Phys. Rev. D **102**, 043006 (2020).

[56] C. A. Raithel, F. Ozel, and D. Psaltis, Finite-temperature extension for cold neutron star equations of state, Astrophys. J. **875**, 12 (2019).

[57] C. A. Raithel, V. Paschalidis, and F. Özel, Realistic finite-temperature effects in neutron star merger simulations, Phys. Rev. D **104**, 063016 (2021).

[58] E. Gourgoulhon, P. Grandclement, K. Taniguchi, J.-A. Marck, and S. Bonazzola, Quasiequilibrium sequences of synchronized and irrotational binary neutron stars in general relativity: 1. Method and tests, Phys. Rev. D **63**, 064029 (2001).

[59] D. Radice and L. Rezzolla, THC: A new high-order finite-difference high-resolution shock-capturing code for special-relativistic hydrodynamics, Astron. Astrophys. **547**, A26 (2012).

[60] D. Radice, L. Rezzolla, and F. Galeazzi, Beyond second-order convergence in simulations of binary neutron stars in full general-relativity, Mon. Not. R. Astron. Soc. **437**, L46 (2014).

[61] D. Radice, L. Rezzolla, and F. Galeazzi, High-order fully general-relativistic hydrodynamics: New approaches and tests, Classical Quantum Gravity **31**, 075012 (2014).

[62] D. Radice, L. Rezzolla, and F. Galeazzi, High-order numerical-relativity simulations of binary neutron stars, ASP Conf. Ser. **498**, 121 (2015), http://aspbooks.org/custom/publications/paper/498-0121.html.

[63] D. Radice, F. Galeazzi, J. Lippuner, L. F. Roberts, C. D. Ott, and L. Rezzolla, Dynamical mass ejection from binary neutron star mergers, Mon. Not. R. Astron. Soc. **460**, 3255 (2016).

[64] D. Radice, General-relativistic large-eddy simulations of binary neutron star mergers, Astrophys. J. Lett. **838**, L2 (2017).

[65] F. Loffler *et al.*, The Einstein Toolkit: A community computational infrastructure for relativistic astrophysics, Classical Quantum Gravity **29**, 115001 (2012).

[66] E. Schnetter, S. H. Hawley, and I. Hawke, Evolutions in 3-D numerical relativity using fixed mesh refinement, Classical Quantum Gravity **21**, 1465 (2004).

[67] C. Reisswig, R. Haas, C. D. Ott, E. Abdikamalov, P. Mösta, D. Pollney, and E. Schnetter, Three-dimensional general-relativistic hydrodynamic simulations of binary neutron star coalescence and stellar collapse with multipatch grids, Phys. Rev. D **87**, 064023 (2013).

[68] M. J. Berger and J. Oliger, Adaptive mesh refinement for hyperbolic partial differential equations, J. Comput. Phys. **53**, 484 (1984).

[69] M. J. Berger and P. Colella, Local adaptive mesh refinement for shock hydrodynamics, J. Comput. Phys. **82**, 64 (1989).

[70] F. Galeazzi, W. Kastaun, L. Rezzolla, and J. A. Font, Implementation of a simplified approach to radiative transfer in general relativity, Phys. Rev. D **88**, 064009 (2013).

[71] C. Reisswig, C. D. Ott, E. Abdikamalov, R. Haas, P. Mösta, and E. Schnetter, Formation and Coalescence of Cosmological Supermassive-Black-Hole Binaries in Supermassive-Star Collapse, Phys. Rev. Lett. **111**, 151101 (2013).

[72] D. Pollney, C. Reisswig, E. Schnetter, N. Dorband, and P. Diener, High accuracy binary black hole simulations with an extended wave zone, Phys. Rev. D **83**, 044045 (2011).

[73] D. A. Godzieba and D. Radice, High-order multipole and binary love number universal relations, Universe **7**, 368 (2021).

[74] D. A. Godzieba, D. Radice, and S. Bernuzzi, On the maximum mass of neutron stars and GW190814, Astrophys. J. **908**, 122 (2021).

[75] J. M. Lattimer and M. Prakash, The equation of state of hot, dense matter and neutron stars, Phys. Rep. **621**, 127 (2016).